

Ultrafast dissipative spin-state dynamics triggered by X-ray pulse trains

Huihui Wang,¹ Tobias Möhle,¹ Oliver Kühn,¹ and Sergey I. Bokarev^{1, a)}

Institut für Physik, Universität Rostock, Albert-Einstein-Str. 23-24, 18059 Rostock, Germany

Frontiers of attosecond science are constantly shifting, thus addressing more and more intricate effects with increasing resolution. Ultrashort pulses offer a practical way to prepare complex superpositions of quantum states, follow, and steer their dynamics. In this contribution, an ultrafast spin-flip process triggered by sub-femtosecond (fs) excitation and strong spin-orbit coupling between 2p core-excited states of a transition metal complex is investigated using density matrix-based time-dependent restricted active space configuration interaction theory. The effect of the nuclear vibrations is incorporated making use of an electronic system plus vibrational bath partitioning. The differences between isolated sub-fs pulses and pulse trains as well as influence of various pulse characteristics on the initiated dynamics are discussed. The effect under study can be potentially used for ultrafast clocking in sub-few fs experiments.

PACS numbers: 31.15.A-; 31.15.aj; 31.15.vj; 32.80.Aa; 33.20.Xx

I. INTRODUCTION

Constant decrease of the duration of light pulses achieved in experiments sharpens the spectroscopic probe used to dissect different atomic and molecular ultrafast processes. This applies not only to nuclear dynamics occurring on the timescale of tens to hundreds of femtoseconds but also to electron dynamics happening about three orders of magnitude faster.^{1,2} In particular, the unprecedented insight into the electron’s “chemistry” has become possible due to development of free-electron lasers and high-harmonic generation sources of ultrashort pulses.³

These pulses have sufficient bandwidth to create a non-stationary superposition of several electronic states and to follow the dynamics of the initiated wavepacket which can be caused both by nuclear and electronic motion. Although experimental developments are only at the beginning of their way, bright prospects are seen and the topic is actively developed by theoreticians (for review see, e.g., Refs. 4–6). For instance, the process of charge migration, where the dynamics of an electronic wavepacket being a superposition of ionized states has been extensively studied theoretically. In this case, the driving force of the dynamics is electron correlation and relaxation. The nuclear motion is argued either to be of minor importance or to cause an ultrafast dephasing destroying coherent electron dynamics. For a discussion of the relevance of nuclear motion for the early-time electron dynamics, see, e.g., Refs. 7–11.

Recently, ultrafast electron dynamics driven by strong spin-orbit coupling (SOC) in the 2p core-excited states of an iron complex have been reported.^{12,13} Remarkably, the dynamics occur on a timescale faster than the Auger decay lifetime of few femtoseconds. These studies considered excitation by a single isolated X-ray pulse, thus, resembling a free electron laser experiments. However,

the experimental realization with a High Harmonic Generation (HHG) setup would require additional effort to obtain such isolated pulses if compared to trains of pulses which are more common in this case.¹ Therefore, in the present work, we extend previous studies for the exemplary case of Fe²⁺ in its first solvation shell along two lines: First, we consider the dynamics driven by trains of ultrashort pulses, which are easier to generate in HHG experiments. Second, we examine the decoherence caused by nuclear vibrations. To this end, a system (electronic degrees of freedom)/bath (nuclear degrees of freedom) model is introduced, whose dynamics is treated using a Quantum Master Equation. In Sec. II, the general framework of the employed time-dependent formalism is presented, followed by the description of computational details in Sec. III. The consequences of dissipation caused by the vibrational bath as well as dynamics caused by series of pulses are discussed in Sec. IV. Conclusions and outlook are given in Sec. V.

II. THEORY

In the following, we make use of the Born-Oppenheimer approximation, thus assuming that the system is excited far from conical intersections. The actual dynamics are studied at a single geometry of the molecule, assuming vertical excitation by the incoming light. The timescale of the processes discussed here (few femtoseconds) is much shorter than the periods of relevant nuclear vibrations (see discussion in Sec. IV), what builds the basis for the present model.

In order to account at least approximately for a possible influence of molecular vibrations but also for loss channels such as Auger decay, a system-bath approach will be used, i.e. the total Hamiltonian is written as

$$\hat{H}(t) = \hat{H}_S(t) + \hat{H}_B + \hat{H}_{S-B}. \quad (1)$$

Here, $\hat{H}_S(t)$ describes the relevant system, i.e. that part of the electronic degrees of freedom (DOF) whose dynamics is triggered by the X-ray light. The relevant system

^{a)}Electronic mail: sergey.bokarev@uni-rostock.de

is coupled via \hat{H}_{S-B} to some bath with Hamiltonian \hat{H}_B . The dynamics of the relevant system according to the reduced density operator, $\hat{\rho}$, follows from the Quantum Master Equation ($\hbar = 1$)¹⁴

$$\frac{\partial}{\partial t} \hat{\rho} = -i[\hat{H}_S(t), \hat{\rho}] + \mathcal{R}\hat{\rho} + \mathcal{A}\hat{\rho}. \quad (2)$$

Equation (2) assumes that the effect of the system-bath interaction can be treated in second order perturbation theory and invoking the Markov approximation. Here, \mathcal{R} is the dissipation superoperator, which accounts for phase and energy relaxation due to interaction with the vibrational bath and \mathcal{A} accounts for the Auger decay. The framework for the description of the electronic subsystem with the density matrix-based restricted active space configuration interaction (ρ -TD-RASCI) is introduced in Section II A and the construction of \mathcal{R} and \mathcal{A} is described in Section II B.

A. ρ -TD-RASCI

Within the ρ -TD-RASCI method, described elsewhere in detail,^{12,13} see also Refs. 15–17, the reduced density operator is represented in the basis of electronic Configuration State Functions (CSFs), $\{\Phi_j^{(S, M_S)}\}$, with the total spin S and its projection M_S . Note that the relaxation of one-electron molecular orbitals (MO) is not taken into account and CSFs are constructed using a time-independent MO basis, optimized at the restricted active space self-consistent field¹⁸ level prior to propagation. On this level, ρ -TD-RASCI can describe electron correlation-driven processes (see regime III in Ref. 13) analogous to charge migration in ionized species.

The Hamiltonian in the CSF basis reads

$$\begin{aligned} \mathbf{H}_S(t) &= \mathbf{H}_{CI} + \mathbf{V}_{SOC} + \mathbf{U}_{ext}(t) \\ &= \begin{pmatrix} \mathbf{H}_h & 0 \\ 0 & \mathbf{H}_l \end{pmatrix} + \begin{pmatrix} \mathbf{V}_{hh} & \mathbf{V}_{hl} \\ \mathbf{V}_{lh} & \mathbf{V}_{ll} \end{pmatrix} + \begin{pmatrix} \mathbf{U}_h(t) & 0 \\ 0 & \mathbf{U}_l(t) \end{pmatrix}, \end{aligned} \quad (3)$$

where we separated blocks of low- (l) and high-spin (h) basis functions. In Eq. (3), \mathbf{H}_{CI} is the configuration interaction (CI) Hamiltonian matrix containing the effect of electron correlation. SOC is contained in \mathbf{V}_{SOC} , whose matrix elements are calculated in the LS-coupling limit, making use of the atomic mean-field integral approximation.¹⁹ The interaction with the time-dependent electric field, $\mathbf{U}_{s=h,l}(t) = -\vec{\mathbf{d}}_{ss} \cdot \vec{E}(t)$, is taken in semiclassical dipole approximation with the transition dipole matrices $\vec{\mathbf{d}}_{hh}$ and $\vec{\mathbf{d}}_{ll}$ ($\vec{\mathbf{d}}_{hl} = \vec{\mathbf{d}}_{lh} = \vec{\mathbf{0}}$). The electric field, $\vec{E}(t)$, corresponds to a train of ultrashort pulses with temporal positions t_i , polarizations \vec{e} , carrier frequencies Ω and Gaussian envelopes with width σ , modeling HHG output,

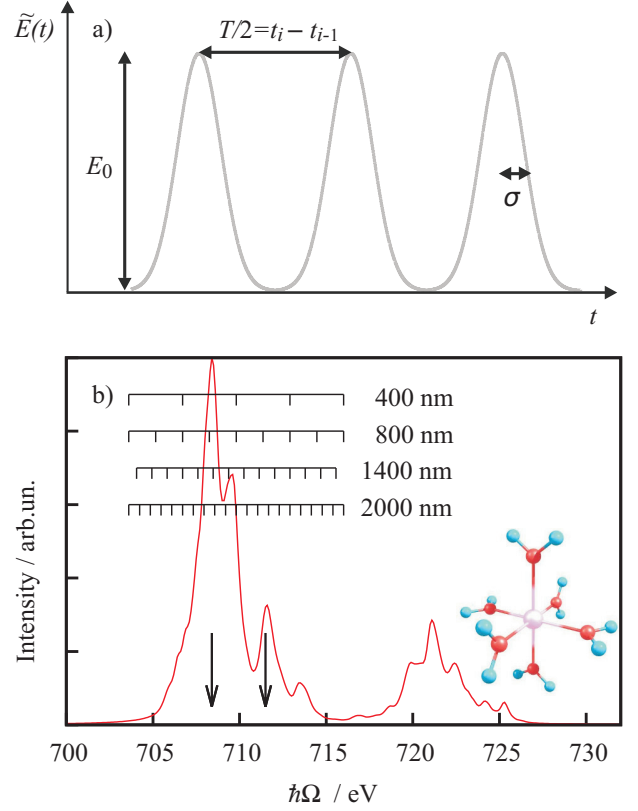


Figure 1. a) Scheme explaining the parameters of the light pulse envelope (Eq. 4); see also Table I. T is the period of the driving laser optical cycle. b) Calculated X-ray absorption spectrum. The energies corresponding to carrier frequencies $\hbar\Omega = 708.4$ and 711.5 eV are marked with arrows. The frequency combs corresponding to HHG with the respective wavelengths of the driving laser are also shown. The structure of the $[\text{Fe}(\text{H}_2\text{O})_6]^{2+}$ complex is presented as an inset.

(cf. Fig. 1a)):

$$\begin{aligned} \vec{E}(t) &= \vec{e}\tilde{E}(t) \cos(\Omega t) \\ \tilde{E}(t) &= E_0 \sum_i \exp(-(t-t_i)^2/(2\sigma^2)). \end{aligned} \quad (4)$$

The delay between two subpulses, $t_i - t_{i-1}$, is determined by the half-period of the optical cycle of the HHG driving laser. The influence of carrier-envelope phase is considered to be irrelevant for the carrier frequency Ω in X-ray range, since multiple oscillations occur within a single pulse in a train.

The eigenstates of \mathbf{H}_{CI} will be called spin-free (SF) states, they are given by the set $\{\Psi_n^{\text{SF},(S, M_S)}\}$. This set can be used to express the eigenstates of $\mathbf{H}_{CI} + \mathbf{V}_{SOC}$, which are called SOC states, as follows:

$$|\Psi_a^{\text{SOC}}\rangle = \sum_n C_{an}^{(S, M_S)} |\Psi_n^{\text{SF},(S, M_S)}\rangle. \quad (5)$$

The notation of the coefficients implies that there is a correspondence $n \leftrightarrow (S, M_S)$. The SOC basis will be

used for representation of the reduced density operator in Eq. (2), which takes the form

$$\begin{aligned} \frac{\partial}{\partial t} \rho_{ab} = & -i\omega_{ab}\rho_{ab} + i\vec{E}(t) \sum_c (\vec{d}_{ac}\rho_{cb} - \vec{d}_{cb}\rho_{ac}) \\ & - \sum_{cd} (\mathcal{R}_{ab,cd} + \mathcal{A}_{ab,cd})\rho_{cd}. \end{aligned} \quad (6)$$

Thus, the time-propagation is performed in the SOC basis which ensures the rigorous structure of the respective equations of motion for the dissipative dynamics leading to proper equilibration.¹⁴ However, the analysis below will also involve the populations of SF states for a certain multiplicity. They are obtained from

$$\rho_{nn}^{(S)} = \sum_{ab} C_{an}^{(S,M_S)} [C_{bn}^{(S,M_S)}]^* \rho_{ab}. \quad (7)$$

B. Dissipation Operators

First, we focus on \mathcal{R} which describes the effect of electron-vibrational coupling. Having in mind the case of a Fe^{2+} ion in its first solvation shell, it is assumed that the vibrations of $[\text{Fe}(\text{H}_2\text{O})_6]^{2+}$ can be mapped onto a harmonic oscillator model. In other words, the vibrational bath is assumed to be a collection of harmonic oscillators in thermal equilibrium coupled to the electronic transitions in a Huang-Rhys like fashion.¹⁴ This constitutes the primary vibrational bath with the interaction operator

$$\hat{H}_{\text{el-vib}} = \sum_{ab} \sum_{\xi} g_{ab,\xi} \omega_{\xi} Q_{\xi} |\Psi_a^{\text{SOC}}\rangle \langle \Psi_b^{\text{SOC}}|, \quad (8)$$

where a and b label the coupled electronic states and Q_{ξ} is the coordinate of the normal mode ξ having frequency ω_{ξ} . Here, $g_{ab,\xi}$ is the dimensionless shift of the a 's state harmonic potential energy surface with respect to the potential of state b , which can be expressed by the Huang-Rhys factor $S_{ab,\xi} = g_{ab,\xi}^2/2$. The coupling strengths $g_{ab,\xi}$ in the SOC basis have been obtained by the transformation of factors $g_{0n,\xi}^{\text{SF}}$, evaluated in the basis of SF states with respect to the ground state $n = 0$, according to Eq. (5). Note that one could further take the non-adiabatic couplings into account explicitly within an approach described in Ref. 20.

This primary bath describing $[\text{Fe}(\text{H}_2\text{O})_6]^{2+}$ is coupled to a secondary one (further solvation shells) leading to a multi-mode Brownian oscillator model.²¹ In total, the effect of primary and secondary bath can be described by the following spectral density

$$J_{ab}(\omega) = \sum_{\xi} \omega_{\xi}^2 g_{ab,\xi}^2 \frac{\omega \omega_{\xi} \gamma}{(\omega^2 - \omega_{\xi}^2)^2 + \omega^2 \gamma^2}, \quad (9)$$

where the parameter γ accounts for the influence of the secondary bath.

Table I. Pulse train characteristics: wavelength of the driving laser λ , delay between two pulses in a sequence $t_i - t_{i-1}$ (see Eq. 4), duration of a single pulse $\sigma = T/14$ and $\sigma = T/28$, where T is the period of the optical cycle of the driving laser

λ , nm	$t_i - t_{i-1}$, fs	$T/14$, fs	$T/28$, fs
400	0.67	0.095	0.048
800	1.33	0.191	0.095
1400	2.34	0.334	0.167
2000	3.34	0.476	0.238

For simplicity we will restrict ourselves to the Bloch model which decouples population relaxation and coherence dephasing. In this case, the only non-zero elements of the relaxation matrix (Redfield tensor) $\mathcal{R}_{ab,cd}$ are given by

$$\mathcal{R}_{aa,cc} = \delta_{ac} \sum_e k_{a \rightarrow e} - k_{c \rightarrow a} \quad (10)$$

for population relaxation and

$$\mathcal{R}_{ab,ab} = \frac{1}{2} \left(\sum_e k_{a \rightarrow e} + \sum_e k_{b \rightarrow e} \right) \quad (11)$$

for coherence dephasing. The relaxation rates $k_{a \rightarrow b}$ for the transition from a state $|\Psi_a^{\text{SOC}}\rangle$ to a state $|\Psi_b^{\text{SOC}}\rangle$, can be expressed as

$$k_{a \rightarrow b} = 2[1 + n(\omega)][J_{ab}(\omega) - J_{ab}(-\omega)], \quad (12)$$

where $n(\omega) = (\exp(\omega/k_B T) - 1)^{-1}$ is Bose-Einstein distribution function.

The Auger autoionization, which for L-edge states of early transition metals is known to dominate the population decay,²² is incorporated phenomenologically by the decay rate Γ_a yielding the simple Auger decay matrix

$$\mathcal{A}_{ab,cd} = -\delta_{ab}\delta_{cd}\delta_{ac}\Gamma_a. \quad (13)$$

Notice that this term is not norm-conserving.

III. COMPUTATIONAL DETAILS

The approach is applied to the spin-dynamics in the core-excited $[\text{Fe}(\text{H}_2\text{O})_6]^{2+}$ complex representing a model of the solvated Fe^{2+} ion, see Fig. 1b). Its X-ray absorption and resonant inelastic X-ray scattering spectra were discussed in Refs. 23–25. The ground electronic state of $[\text{Fe}(\text{H}_2\text{O})_6]^{2+}$ corresponds to the quintet ($S = 2$) high-spin d^6 electronic configuration, which should be triply degenerate if octahedral symmetry is assumed. This degeneracy is lifted due to the weak Jahn-Teller effect leading to the three close-lying electronic states.

CSFs were constructed within a RASSCF (restricted active space self-consistent field) scheme using an active space containing 12 electrons distributed over the three 2p (1 hole is allowed) and five 3d (full CI) orbitals. This

setup is sufficient to describe the core excited electronic states corresponding to the dipole allowed $2p \rightarrow 3d$ transitions.^{23–25} In total, 35 quintet ($S = 2$) and 195 triplet ($S = 1$) electronic states, directly interacting via SOC according to the $\Delta S = 0, \pm 1$ selection rule, were considered. Accounting for the different M_S microstates, the total number of SF and SOC states was 760, with 160 being valence and 600 core ones. Scalar relativistic effects we considered at the second-order Douglas-Kroll-Hess transformation level.²⁶ Time-independent matrix elements in Eq. (3) were evaluated with the MOLCAS 8.0²⁷ program package, applying the ANO-RCC basis set of triple- ζ quality.^{28,29}

The electron-vibrational couplings in the SF basis, $g_{0n,\xi}$, were obtained from the forces at vertical excitation employing a quantum chemical hybrid approach on the basis of the shifted harmonic oscillators model. Here, the force constant matrix was determined at the level of DFT/B3LYP/6-311G(d) for the ground state and the gradients in the excited electronic states were computed at the ground state geometry using the RASSCF method as described above. The width γ in the spectral density, Eq. (9), accounting for the interaction between the modes of the solvated ion and further degrees of freedom of the environment, was set to 500 cm^{-1} for all normal modes. The rates Γ_a , phenomenologically accounting for Auger decay, were set to 0.4 and 1.04 eV for the L_3 and L_2 edges, respectively.³⁰ These values correspond to lifetimes of the core hole of 10.3 and 3.98 fs.

Equation (2) was solved using the Runge-Kutta-Fehlberg integrator with adaptive step size varying from 2.5 as down to 0.09 as depending on the field strength. The initial density matrix was populated according to the Boltzmann distribution at 300 K:

$$\rho_{ab}(0) = \delta_{ab} \exp(-E_a/kT) / \sum_c \exp(-E_c/kT). \quad (14)$$

The parameters E_0 , t_i and σ in Eq. (4), determining the shape of the time-dependent external electric field, were chosen to roughly resemble the regimes of the commonly used driving laser systems for the generation of high harmonics. However, some assumptions on the form of the incoming electric field have been done allowing to simplify the computational protocol. For the wavelength of the driving laser, we have chosen 800 nm corresponding to the Ti:Sapphire laser as well as 400, 1400, and 2000 nm, which can be obtained by frequency doubling and parametric amplifiers of the 800 nm laser. These values correspond to shifts between consecutive sub-pulses $t_i - t_{i-1}$ from about 1 to 7 fs, see Table I. Ten pulses have been considered in each series assuming equal envelopes of the subpulses for simplicity. The simulations have been carried out for two field amplitudes, E_0 , of 2.5 and 0.25 a.u. for each pulse comb. Note that despite the large values of E_0 , at soft X-ray wavelength this corresponds to the weak field regime, see Refs. 12,13. The polarization vector \vec{e} has been chosen to be parallel to the shortest Fe–O bond of the $[\text{Fe}(\text{H}_2\text{O})_6]^{2+}$ complex. It

should be noted that the trains of ultrashort pulses in our theoretical study have been designed solely for illustration purposes and correspond to realistic experimental setups only approximately. However to the best of our knowledge, such a setup is not yet available. The real carrier frequencies used have not been set to particular harmonics of the driving laser and for convenience corresponded to maxima of two peaks in absorption spectrum (708.4 and 711.5 eV, cf. Fig. 1b)), considered before, see Refs. 12,13. Fig. 1b) also contains the HHG frequency combs generated with different lasers overlaid with the spectrum. One can see that the chosen “resonant” carrier frequencies only slightly differ from the exact positions of the harmonics apart from the case of 400 nm driving laser. The widths σ in Eq. (4) have been chosen as $T/14$ and $T/28$, where T is the period of optical cycle of the driving laser. Here we assume that the parameter σ can be controlled filtering out the low-energy harmonics of the HHG output. (Otherwise, it would be bound to the inverse of the cutoff energy.) The pulse characteristics are summarized in Table I.

IV. RESULTS AND DISCUSSION

A. Role of electron-vibrational coupling

In order to obtain an overview with respect to the effect of electron-vibrational coupling, we have calculated one-dimensional cuts of the potential energy surfaces (PES) along the symmetric Fe–O breathing mode ($\xi = 15$), which is the most strongly coupled mode (see below). Results are shown in Fig. 2, with the color code indicating the change of multiplicity of the respective states from quintet (red) to triplet (blue). Panels a) and c) correspond to PES of core- and valence-excited electronic states, respectively, in the SF basis. The results for the SOC state representation are shown in panels b) and d).

The states at lower energy are of quintet character in all cases. For the valence excited states this is followed by a band of triplet states, with some occasional mixing between triplet and quintet states in the SOC basis in the vicinity of intersection points. We also notice that triplet states cross each other. Since the selected mode is of tuning-type it can be anticipated that there are coupling modes, which render these crossings into conical intersections. Overall, the treatment of the dynamics in the valence excited states would require sophisticated wave packet propagation.

The situation is rather different for the core-excited states, in particular, concerning the SOC state PES, which are of main interest here. Due to the large value of the SOC ($|V_{\text{SOC}}| = 8.5 \text{ eV}$) there are substantial energy shifts if panels a) and b) are compared. In addition, there is a splitting of the M_S -components, leading to an almost continuous density of states (especially in energy region 708–711 eV which will be used for excitation below). In passing, we notice that in panel c) one can still observe

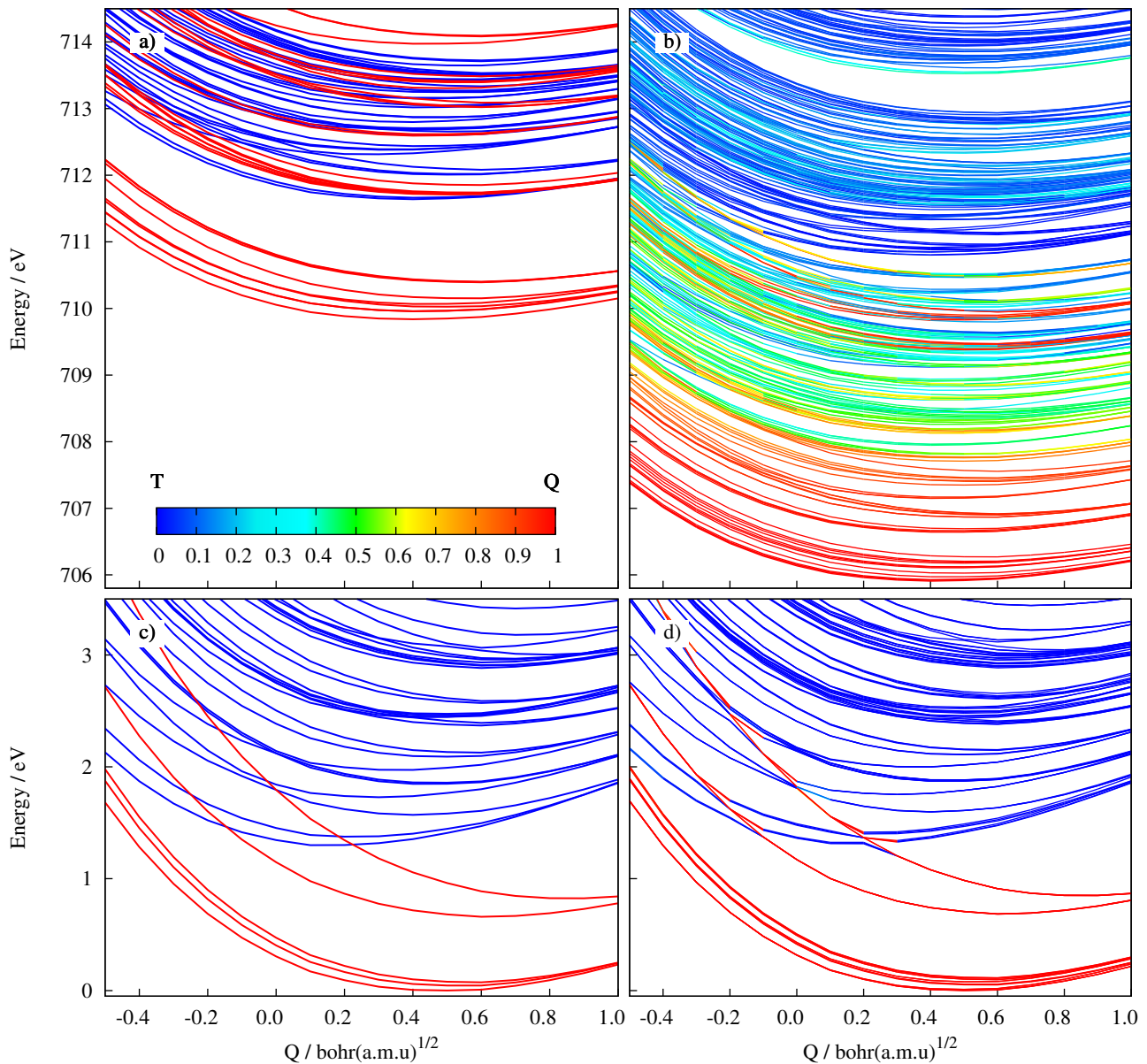


Figure 2. The cuts of the potential energy surfaces along the most active tuning vibrational mode (ground state frequency 417 cm^{-1}). Panels a) and c): core and valence PESs of quintet SF states (red lines) and triplet SF states (blue lines), respectively, in the SF basis. Panels b) and d): same PESs in SOC basis, the color of lines corresponds to the collective contribution $\sum_{n, M_S} |C_{an}^{(S=2, M_S)}|^2$ of all quintet ($S = 2$) SF states to a particular $|\Psi_a^{\text{SOC}}\rangle$, see Eq. (5). Note that only a part of states is shown in panels a) and b), corresponding mainly to the L_3 absorption band. Also note that due to the hybrid approach (DFT ground state geometry and RASSCF PES) the minima of the ground state PES is not at zero.

a certain pattern with respect to the multiplicity of the states, which changes from quintet via strongly mixed to triplet with increasing energy.

From this picture one can draw two conclusions: First, SOC is the dominant coupling mechanism, making electron-vibrational coupling a small perturbation at short times. This justifies the use of a Markovian Quantum Master Equation for the description of the effect of electron-vibrational coupling. Second, due to the essentially continuous density of states it can be expected that

details of the electron-vibrational interaction will only be of minor importance. Although the SF PES are manifestly anharmonic, the harmonic approximation in conjunction with the Huang-Rhys model might still give a reasonable estimate for the electron-vibrational coupling constants. In fact, one might view the present approach as providing a simple kinetic approach to the influence of electron-vibrational coupling on the spin-flip dynamics.

Analysis of Huang-Rhys factors in the SF basis, $g_{0n, \xi}^2/2$, shows that only few vibrational modes out of

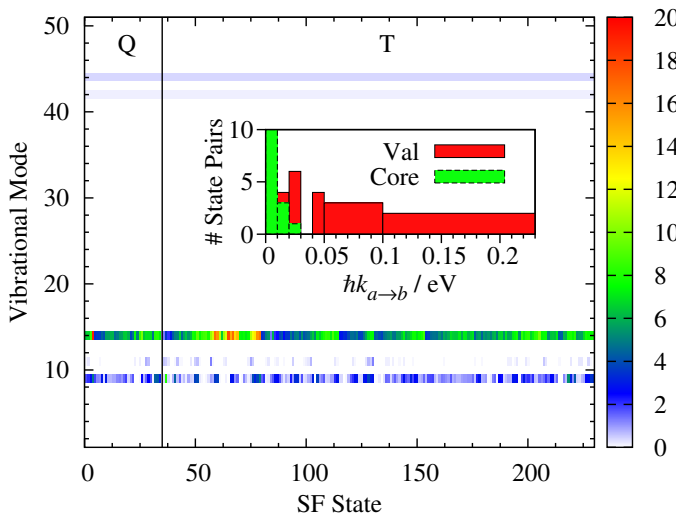


Figure 3. Huang-Rhys factors, $g_{0n,\xi}^2/2$, for the transitions from the ground to the quintet (Q) and triplet (T) SF states for all 51 vibrational modes ξ . Inset: Distribution of relaxation rate $\hbar k_{a \rightarrow b}$ values (Eq. (12)) for different pairs (a, b) of valence and core SOC states. (Note that the first column of the histogram is cut at the value of 10.)

the 51 possible ones are active, see Fig. 3. Most prominent shifts between harmonic oscillators for both quintet and triplet as well as valence- and core-excited states correspond to two modes ($\xi = 10$ and 15) with ground state frequencies of 228 and 417 cm^{-1} , which are of Fe-O stretching type. This is not surprising since only oxygen 2p orbitals are strongly mixing with 3d orbitals of iron and thus both 3d-3d and 2p-3d electronic transitions are influenced by the distance to oxygens and are almost insensitive to vibrations of water ligands themselves. Nevertheless, some other vibrations like symmetric O-H stretching modes at 3640 cm^{-1} ($\xi = 43$) and 3645 cm^{-1} ($\xi = 45$) also have non-vanishing magnitudes, but do not play a major role.

The rates calculated according to Eq. (12) are summarized in a histogram shown as an inset in Fig. 3. Out of 288420 possible state pairs and thus transition rates, only few are larger than 0.01 eV. Remarkably, energy dissipation due to transitions between valence states is more prominent than that between core excited states.

The population dynamics for the selected valence and core SF and SOC states is presented in Fig. 4. These states have been selected to show the effect of the largest dissipation rates. To simplify the analysis, the regime of excitation corresponds to the single 132 as pulse, resembling that used in Ref. 12, and neglecting Auger decay. Due to the spectral bandwidth of ultrashort pulse many core states are excited. The typical populations of individual states are comparable to that shown in Fig. 4a. The populations of valence SF states show oscillations typical for zero-order states building up a superposition in case of small coupling between them. The core SF states in turn exhibit a more intricate pattern which can

be explained by much stronger coupling and larger state density. The eigenstates of the SOC Hamiltonian are stationary as soon as the pulse is over and no dissipation is accounted for. Interaction with the vibrational bath causes notable population transfer between state pairs with largest $k_{a \rightarrow b}$. However, due to the small amount of such pairs with $\hbar k_{a \rightarrow b} > 0.01$ eV which are essentially responsible for energy dissipation to the vibrational bath, such a relaxation does not play decisive role at least at the timescale of 15 fs which is very small if compared to typical period of Fe-O stretching vibrations (> 100 fs). Although the populations of the particular states with the largest $k_{a \rightarrow b}$ are notably affected by the dissipation as is illustrated in Fig. 4, the populations of these states themselves are quite small what does not lead to notable differences in the dynamics of the total populations of quintet and triplet states (compare magnitudes of populations with Fig. 5a).

Summarizing, within our model the SOC driving force (which is electronic in its nature) of the ultrafast spin flip is by far dominating over the effect of electron-vibrational coupling. Essentially, the population relaxation due to vibrations can be neglected especially taking into account the ultrashort time period considered. Importantly, the dephasing caused by coupling to the nuclear bath is not destroying the coherence initially created by the absorption of the ultrashort pulse. The last statement, however, requires a note of caution. In our study, we did not account for the width of nuclear wave packet in the initial state which can also cause ultrafast dephasing.^{9,11,31}

B. Multipulse excitation

It has been shown previously that a single intense soft X-ray pulse can cause an unprecedented ultrafast spin flip.^{12,13} An illustration for this process is given in Fig. 5a. Here, the total populations (Q(tot) and T(tot)) of quintet, $\sum_n \rho_{nn}^{(S=2)}$, and triplet, $\sum_n \rho_{nn}^{(S=1)}$, SF states are shown as a function of time. In addition, the overall populations of valence and core quintet and triplet states are given, where summation over n is performed only within the respective manifolds. One can see that an isolated pulse with duration 132 as initially excites the system to the quintet core manifold and subsequently the population transfers to the triplet manifold on the timescale of few fs due to strong SOC. This process is purely electronically driven and occurs even when the nuclei are fixed and no coupling to the vibrational bath is accounted for.^{12,13}

Since isolated few-femtosecond and sub-femtosecond pulses require special techniques to be obtained,¹ we have investigated what happens if pulse trains are applied. The parameter space ($\lambda, \sigma, E_0, \hbar\Omega$) of these pulse bursts (see Section III) has been systematically screened. In the following, we discuss the main trends on the basis of few illustrative examples shown in Figs. 5b-f) and 6; more results can be found in the Supplement. Both figures focus on two driving laser wavelengths, i.e. 800 nm and

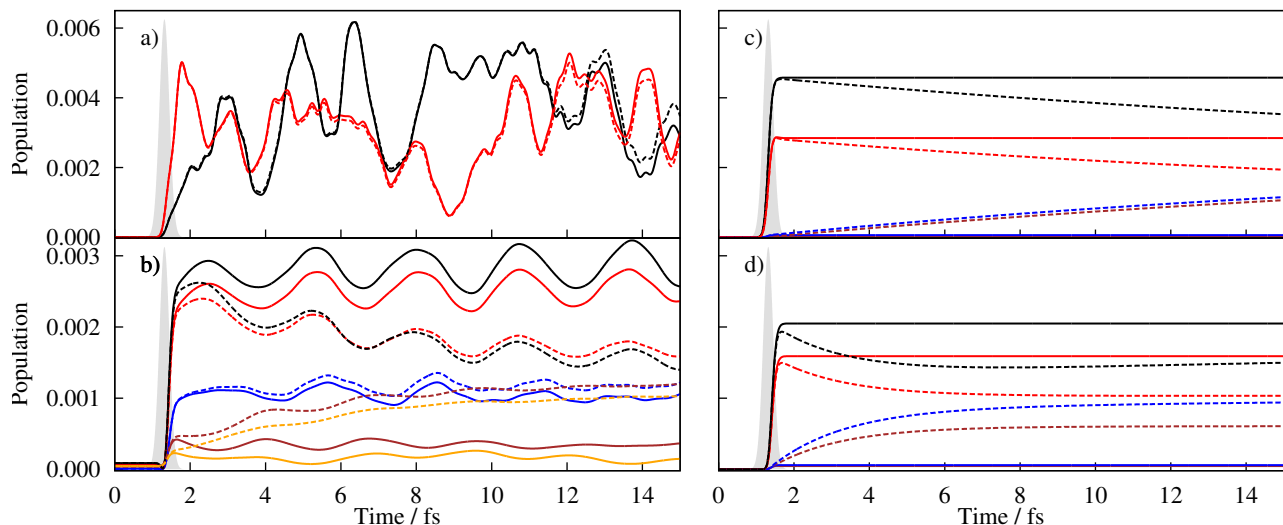


Figure 4. Population of selected states corresponding to the largest relaxation rates (cf. Fig. 3) with (dash lines) and without (solid lines) bath. a) core SF states; b) valence SF states; c) core SOC states; d) valence SOC states. The envelope of the excitation pulse is shown as a grey-shaded area.

2000 nm. The first one corresponds to the most common Ti:sapphire laser, typically used for HHG experiments, whereas the second is available via parametric amplifiers and should allow for higher cutoff energies possibly reaching soft X-ray range with higher intensity. Note that λ actually fixes the interpulse delay to the half of period. Moreover, in our model, the duration of individual subpulses has been chosen to depend on the period ($\sigma = T/14$ and $T/28$) and thus λ itself, see Sec. III. This makes the wavelength of the driving laser the most important parameter in our simplified model. Further, to address the field strength dependence, the results are presented for $E_0 = 2.5$ a.u. and 0.25 a.u. with respective intensities 8.8×10^{16} and 8.8×10^{15} W/cm². The carrier frequencies of $\hbar\Omega = 708.4$ (Fig. 5) and 711.5 eV (Fig. 6) correspond to the maxima of two peaks in L₃-edge absorption spectrum of aqueous Fe²⁺ ion, see Fig. 1b).²⁵ These regions resemble different spin-orbit coupling regimes, see for instance Ref. 12. At 708.4 eV the prepared superposition of states contains more quintet SF states, whereas at 711.5 eV more triplet ones as is apparent from Fig. 2b).

Looking at the results in Figs. 5c)-f) and 6 one can see that the pulse trains essentially demonstrate similar effects on the spin dynamics of the system as the isolated pulses (cf. Fig. 5a), but with a number of differences. First, there are prominent ultrafast dynamics happening between individual pulses in a train. It is most obvious in case of high field intensities. These dynamics corresponds to the field-free evolution of the coherent electronic wave packet created by a single pulse. As a result the population of SF quintet states drops down and that of SF triplet states increases between pulses. Note the close similarity between the initial region of the population curves, e.g., in panels a) and c) of Fig. 5.

Second, a remarkable feature of the dynamics is the

stepwise pumping of the triplet population with each new incoming subpulse if $E_0 = 2.5$ a.u. is used. In general, the height of the steps is almost monotonously decreasing with every next pulse and the population approaches a plateau, which only slightly depends on the pulse characteristics and in most cases amounts to around 0.7. For instance, for $\lambda = 800$ nm and 2000 nm and $E_0 = 2.5$ a.u. the first five or six pulses correspond to largest steps in triplet population growth and subsequent ones lead to relatively minor changes in population, comparable to those of free dynamics (panel 5a)). Thus, every next subpulse increases the triplet yield, if only final populations are in focus. Observing the stepwise behavior in experiment would, however, require a pump-probe setup, what makes such an observation challenging.

In some cases, valence excited states gain substantial population. For instance, valence triplet states constitute up to 35% of the total triplet population. This effect may be clearly seen in the changes of populations during pulses with $E_0 = 2.5$ a.u., where both triplet and quintet valence populations may rise during the pulse, and may be attributed to stimulated emission. However, this effect may be considered as being of limited practical relevance, since it requires very high field strengths.

The character of the dynamics changes quite notably when the strength of the pulses is decreased by a factor of ten (Fig. 5d) and f) as well as Fig. 6b) and d)). In this case, the contribution from stimulated emission is barely seen, apart from panel 5f). The behavior of the system shows a much more regular stepwise pumping with the sizes of the steps being almost constant and much smaller than for the stronger fields. The yield of triplet states in most cases stays below that of quintet states, with the examples shown in panels 5b) and 5d) being rather an exception (see, e.g., Fig. 7). The qualitative behavior of

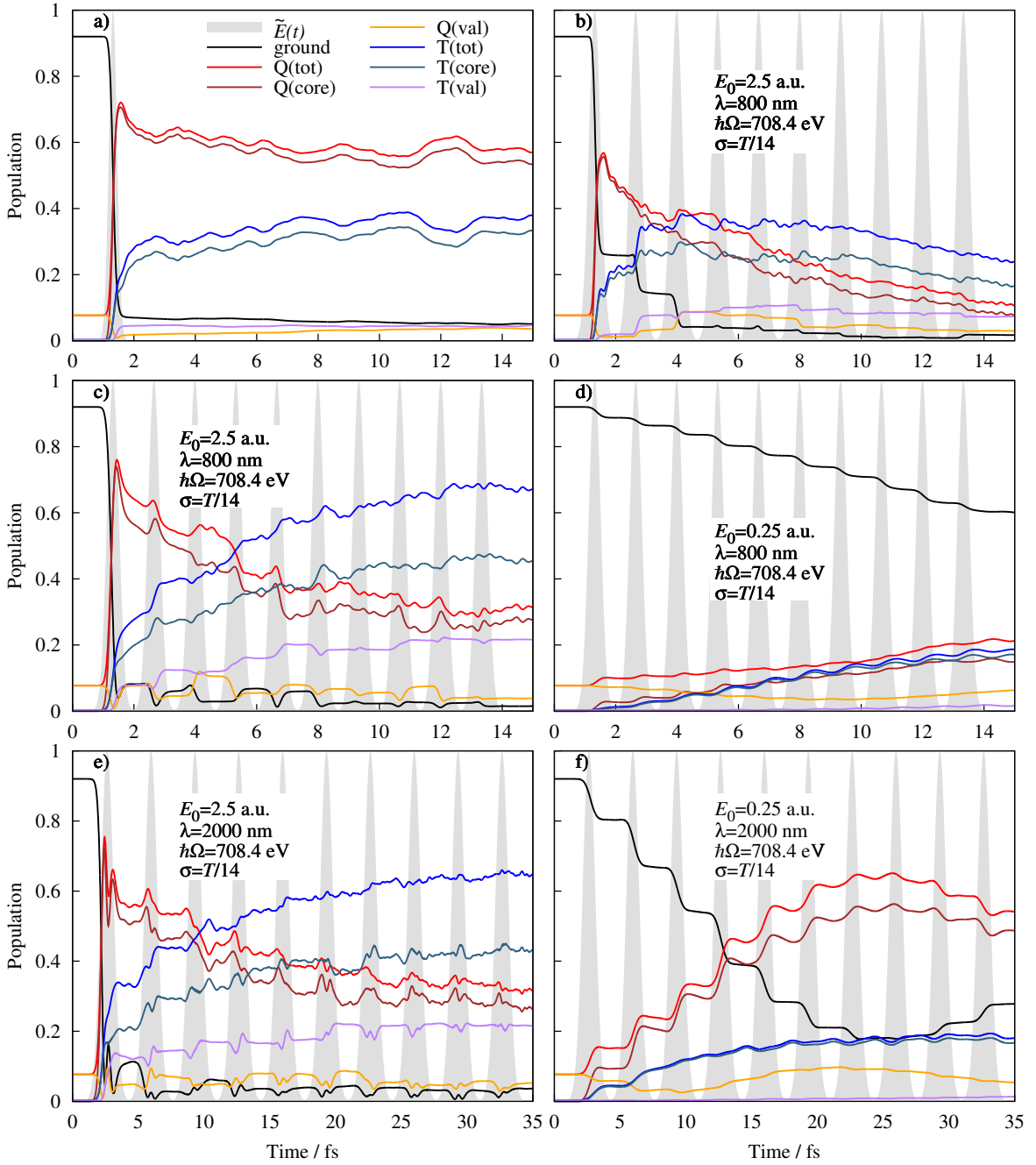


Figure 5. Spin dynamics initiated by pulse trains having different characteristics: The shape of the normalized pulse envelope $\tilde{E}(t)/E_0 = \sum_i \exp(-(t-t_i)^2/(2\sigma^2))$ is depicted with grey filled curves. The populations of electronic SF states are presented for the cases of total quintet, Q(tot), and triplet, T(tot), as well as of the respective valence, Q(val) and T(val), and core, Q(core) and T(core). The black curve corresponds to the population of the lowest quintet (ground) state; note the finite temperature of 300 K resulting in an initial population of 0.92. The amplitude E_0 , wavelength of the driving laser λ , carrier frequency (energy) $\hbar\Omega$, and subpulse duration σ are given in the respective panels. The dissipation due to vibrational bath is included. Panel a): Dynamics initiated by a single pulse ($E_0 = 2.5$ a.u., $\hbar\Omega = 708.4$ eV, $\sigma = 132$ as), no vibrational bath, no Auger decay. Panel b): Example of dynamics accounting for Auger decay. Panels: c)-f) Auger decay is excluded for simplicity of the analysis.

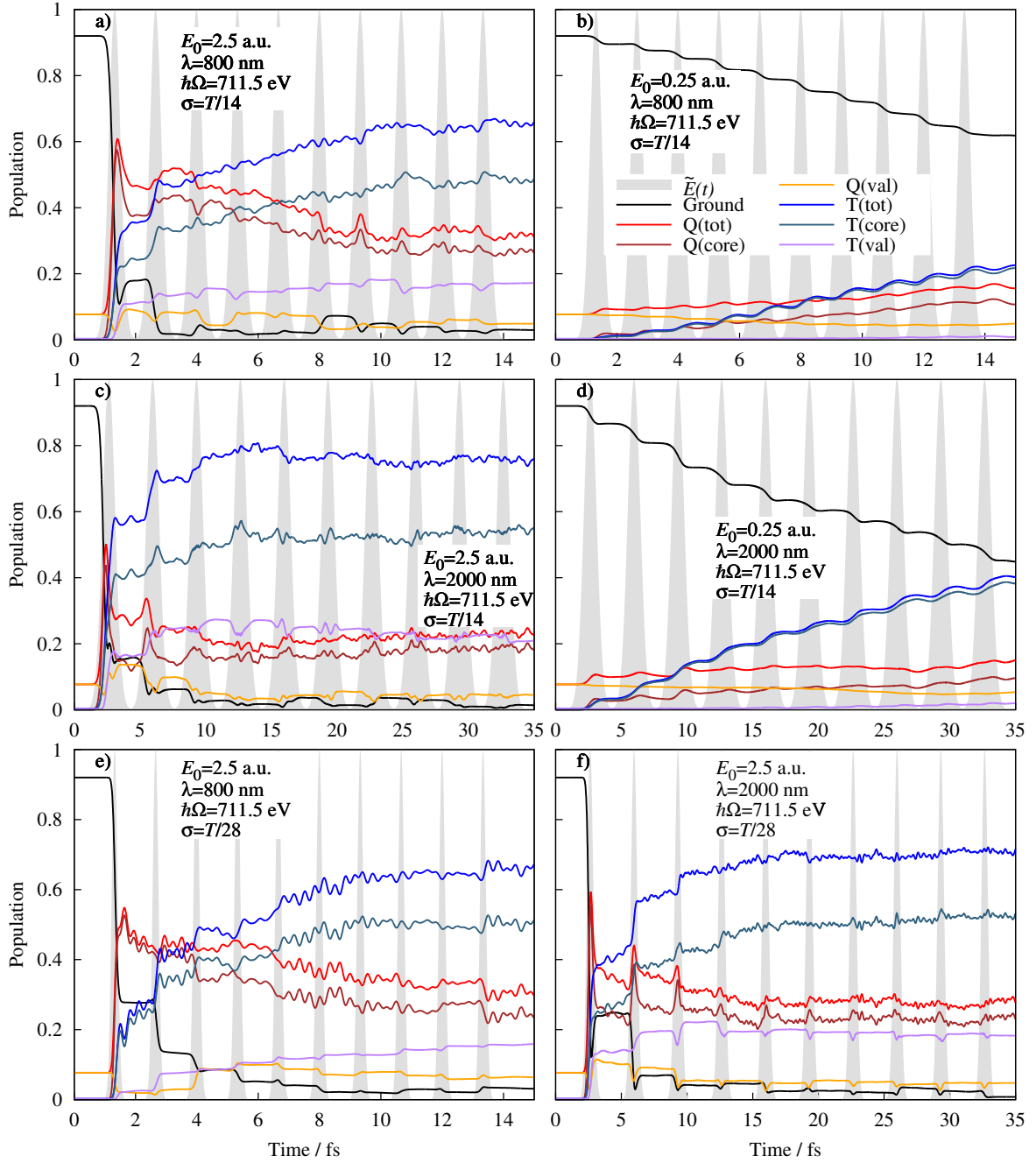


Figure 6. Spin dynamics initiated by pulse trains having different characteristics as given in the panels; see also Fig. 5.

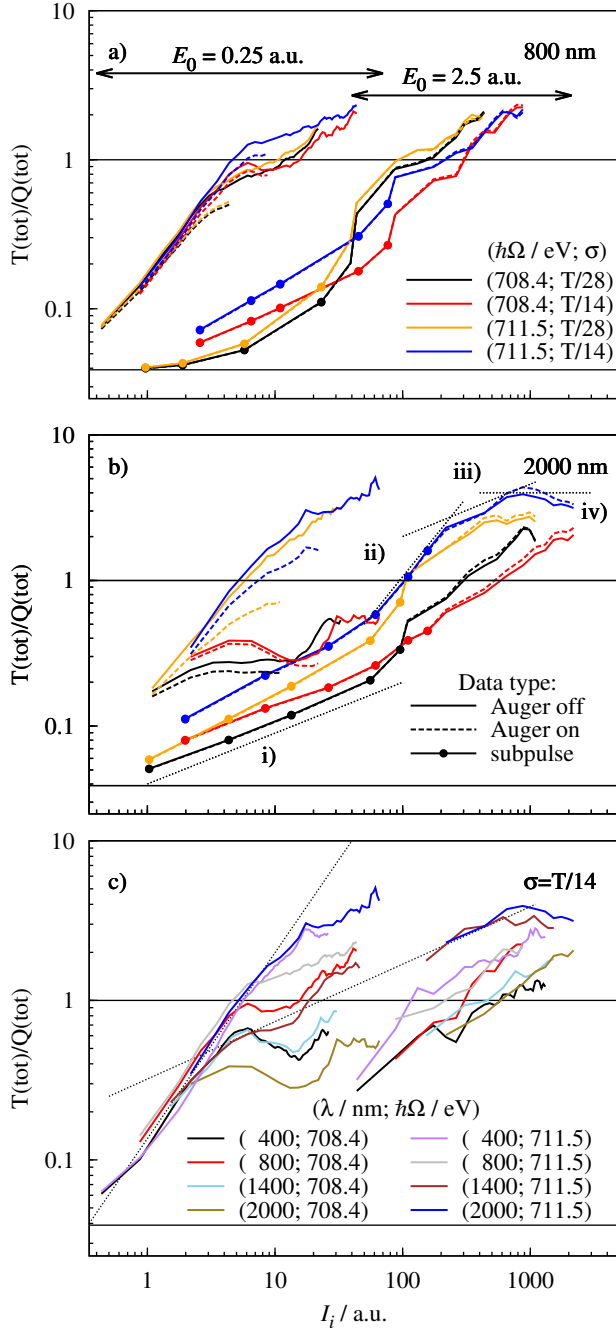


Figure 7. Relative yield of the total triplet population, $T(\text{tot})$, with respect to the total quintet one, $Q(\text{tot})$, versus the integrated intensity envelope $I_i = \int_{-\infty}^{(t_{i+1}-t_i)/2} |\tilde{E}(t)|^2 dt$. Here, the time $(t_{i+1}-t_i)/2$ corresponds to end of the i th subpulse in a train before $i+1$ th subpulse starts. Panels a) and b) correspond to $\lambda = 800$ and 2000 nm . The population dynamics with/without Auger decay are shown as solid/dashed lines, respectively. For $E_0 = 2.5 \text{ a.u.}$ in panels a) and b), the first subpulse in the sequence is split into parts to ensure the overlap of two groups of curves along the I_i -axis, see text. The respective data are shown with filled circles. In panel c), the results for different λ are presented for $\sigma = T/14$. Two horizontal lines denote the starting $T(\text{tot})/Q(\text{tot})$ and the point of $T(\text{tot})=Q(\text{tot})$.

quintet and triplet populations with respect to each other is not changed when Auger decay is included apart from the double-exponential total decay (see Fig. 5b as well as Supplement).

One can also analyze the dynamics in terms of the integral intensity (energy) transferred from the pulse to the system. For this purpose, we have plotted in Fig. 7 the total triplet yield relative to the total quintet population, $T(\text{tot})/Q(\text{tot})$, versus the integrated intensity envelope $I_i = \int_{-\infty}^{(t_{i+1}-t_i)/2} |\tilde{E}(t)|^2 dt$. Here, i runs over individual pulses in a train and, thus, the triplet yield after every subpulse is plotted. The data represent two groups of curves for $E_0 = 0.25$ and 2.5 a.u. which are barely overlapping along the intensity axis if integer number of pulses is considered. To compare the triplet yield for both E_0 at the same value of integrated intensity, we have split the first pulse in the sequences with $E_0 = 2.5 \text{ a.u.}$ into pieces of shorter duration (and thus smaller intensity). The respective data points are depicted by the filled circles in Fig. 7a) and b). The data with Auger decay taken into account are plotted as dashed lines; these data sets included always 10 pulses in a train. For dynamics without Auger effect and 0.25 a.u. field amplitude, longer pulse sequences are applied again to increase the overlap in integrated intensity with stronger pulses. Further, results for different λ and $\hbar\Omega$ are given in panel c) for $\sigma = T/14$.

The dependencies in Fig. 7 can be roughly subdivided into several almost linear regions (see Fig. 7b); note the double logarithmic scale): i) initial one, mainly seen during the first pulse for $E_0 = 2.5 \text{ a.u.}$; ii) linear rise with high steepness most apparent for $E_0 = 0.25 \text{ a.u.}$; iii) rise with lower steepness; iv) saturation region which can be followed by decrease or oscillatory behavior of the T/Q ratio. The region iii) with lower steepness begins when the triplet population starts to dominate the quintet one. That is why it can be attributed to the interplay of the absorption/emission and $Q \rightarrow T/T \rightarrow Q$ forward and backward processes, thus, decreasing the rate of the spin crossover. Remarkably, the steepness of the linear regions i)-iii) is quite similar for different pulse characteristics, see, e.g., Fig. 7c). Similarity of all dependencies underlines the statement that the essential dynamics does not crucially depend on the pulse strength what justifies selection of high intensities for illustration purposes.

Pulse duration or associated bandwidth has also an influence on the dynamics. In general, shorter durations ($\sigma = T/28$) cause faster oscillations than the longer ones ($\sigma = T/14$), compare 6a) and 6c) with 6e) and 6f). This can be rationalized by the larger bandwidth and thus involvement of more energetically distant states in the superposition. Naturally, since E_0 is the same for both durations, shorter pulses have smaller area under the $|\tilde{E}(t)|^2$ curve and thus are effectively weaker than the longer ones (note the shift along x -axis in Fig. 7).

Interestingly, pulse-train excitation with weaker fields shows more variability than with stronger ones. This applies both to time-dependences of populations (Figs. 5

and 6) and integral intensity picture (Fig. 7). For weaker pulses, the system is not kicked that hardly and evolution is closer to its natural dynamics. This is not the case if trains of pulses with $E_0=2.5$ a.u. are used. Here, populations of all kinds of states show a similar pattern across the pulse parameter space. Importantly, at both carrier frequencies triplet population exceeds the quintet one reaching a plateau at similar values. In contrast, weaker pulses ($E_0 = 0.25$ a.u.) initiate the dynamics that are much more similar to those triggered by a single pulse.^{12,13} For instance, two carrier frequencies ($\hbar\Omega = 708.4$ and 711.5 eV) and pulse durations ($\sigma = T/14$ and $\sigma = T/28$) correspond to different yields of triplet states. However in general, one can say that dynamics driven by a series of pulses seems to be less dependent on the characteristics of a particular pulse in a train than in case of isolated pulses.

A possible explanation could be that a single pulse creates a coherent superposition which evolves in time according to the full Hamiltonian in Eq. (3), while multiple pulses constantly prepare new superpositions smearing out the populations over core- and valence-excited states in course of absorption and stimulated emission. This smearing over states with different energies makes the overall dynamics having less dependence on the position of the center and bandwidth of the incoming field envelope in the frequency domain. It could also be the reason for the plateau-like behavior of the triplet populations in case of the stronger field.

Surprisingly, the delay between consecutive pulses has also quite moderate influence on the dynamics. Only for $\lambda = 400$ nm the pattern of the fast oscillations notably changes. It corresponds to the shortest pulses used in this work meaning the largest bandwidth in the frequency domain. The ultrafast oscillations with a period of 0.32 fs can be then attributed to the superposition of the most distant states split due to SOC by 12.7 eV.

Finally, the leak of the norm due to Auger process is very fast (Fig. 5b)), corresponding to biexponential decay with time constants 3.98 and 10.34 fs in accordance with our phenomenological model (Eq. (13)). Despite of this fast decay, the spin-flip process is still faster leading to a behavior similar to that discussed above. The only difference is that in this case the total triplet population is lower and is decaying with the slow Auger component. In this respect, depositing population into valence triplet manifold enabled by stimulated emission decreases the destructive effect of the Auger decay on the spin-flip efficiency. This scenario, however, would require very intense fields which are not yet achievable in practice.

The same conclusions can be drawn from Fig. 7. There, the Auger decay naturally shows up for longer times (larger number of subpulses) and that is larger integrated intensities. At the beginning (region ii)) the population curves with and without Auger autoionization almost coincide and the divergence becomes more obvious for large intensities. Interestingly, Auger decay has a major effect for sequences of weak pulse ($E_0 = 0.25$ a.u.), where it

tends to notably decrease the triplet yield. For stronger fields, the effect is smaller and, in contrast, the triplet yield increases.

Summarizing, weak pulses are more selective. Further, for a particular integrated intensity without Auger decay, they are more efficient than the stronger ones if we compare triplet yields for a fixed I_i (Fig. 7). Accounting for the fact that they are more readily available in experiment, this makes them the most suitable candidates to address or steer ultrafast spin dynamics. This effect is, however, counterbalanced by the destructive influence of Auger decay. On the other hand, from the viewpoint of the time of the spin crossover, stronger pulses should be more efficient as they lead to faster increase of triplet population. In this case, the Auger effect is less important because of faster spin-flip transitions and involvement of non-decaying valence states via stimulated emission.

V. CONCLUSIONS

This study represents an extension of the analysis of ultrafast spin-flip dynamics reported before.^{12,13} The main two questions addressed here are: Does the coupling of the electronic subsystem to nuclear vibrations alter the dynamics? What changes if pulse trains are used instead of a single pulse?

The former problem is treated at the level of system-bath partitioning. This approach corresponds to an approximate scheme since no non-adiabatic coupling is taken into account explicitly. Moreover, the width of nuclear distribution in the ground state is not accounted for. The bath is represented essentially by a single damped totally-symmetric vibrational mode which is strongly coupled to the electronic states. The effect of energy dissipation and decoherence is taken into account using a simple Bloch model. The computed rates are very small in comparison to the strength of SOC. Moreover, the state pairs which are notably coupled by the symmetric stretching mode are very small in number. Therefore, within our dissipative model, the vibrational bath does not play prominent role on dynamics at least at the considered time-scale below 50 fs.

Further, the effect of the multi-pulse excitation typical for HHG setups has been simulated. Parameters of the pulses have been chosen to roughly resemble possible experimental setups. The net effect of interaction with pulse trains is in general analogous to isolated pulse excitation. Most important is that ultrafast spin-flip also occurs for multiple pulses. Even more, utilizing bursts makes the process more efficient leading to a stepwise pumping of triplet population. Interestingly, the differences in dynamics caused by intense pulses show less sensitivity to individual pulse characteristics such as carrier frequency, duration, and interpulse delay. Weaker pulses are more selective and in some cases show no predominant population of spin-flipped states.

The effect, studied here theoretically, calls for experimental observation. Our study suggests that the light characteristics needed to trigger this effect are within reach. We are confident that further development of non-linear X-ray spectroscopic techniques such as stimulated resonant inelastic X-ray scattering⁶ or employment of magnetic circular dichroism probe within a pump-probe experiment will enable measuring ultrafast spin-flip dynamics.

Although it is of fundamental interest to address ultimate timescale of electron dynamics caused by spin-orbit coupling, we envisage that this effect could be used for clocking ultrafast events. In this respect, it is of core-hole clock type³² but has a different nature. Moreover, in case of spin-flips the characteristic timescale may be varied by addressing different atoms in the system or various types of core holes as well varying the carrier frequency and bandwidth of the incoming radiation, thus adjusting the strength of the coupling and thereby determining essentially the measured time window.

ACKNOWLEDGMENTS

The authors would like to acknowledge the fruitful discussion with Prof. Dr. Stefan Lochbrunner (University of Rostock) as well as financial support from the following sources: Deanship of Scientific Research (DSR), King Abdulaziz University, Jeddah, grant No. D-003-435 (H.W. and O.K.), Landesgraduiertenförderung of Mecklenburg-Vorpommern (T.M.), and Deutsche Forschungsgemeinschaft grant No. BO 4915/1-1 (S.I.B.).

REFERENCES

- ¹T. Schultz and M. Vrakking, eds., *Attosecond and XUV Physics: Ultrafast Dynamics and Spectroscopy* (Wiley-VCH, Weinheim, 2014).
- ²F. Lépine, G. Sansone, and M. J. Vrakking, *Chem. Phys. Lett.* **578**, 1 (2013).
- ³L. Young, K. Ueda, M. Gühr, P. H. Bucksbaum, M. Simon, S. Mukamel, N. Rohringer, K. C. Prince, C. Masciovecchio, M. Meyer, A. Rudenko, D. Rolles, C. Bostedt, M. Fuchs, D. A. Reis, R. Santra, H. Kapteyn, M. Murnane, H. Ibrahim, F. Légaré, M. Vrakking, M. Isinger, D. Kroon, M. Gisselbrecht, A. L’Huillier, H. J. Wörner, and S. R. Leone, *J. Phys. B* **51**, 032003 (2018).
- ⁴A. S. Moskalenko, Z.-G. Zhu, and J. Berakdar, *Phys. Rep.* **672**, 1 (2017).
- ⁵A. I. Kuleff and L. S. Cederbaum, *J. Phys. B* **47**, 124002 (2014).
- ⁶Y. Zhang, W. Hua, K. Bennett, and S. Mukamel, *Top. Curr. Chem.* **368**, 273 (2015).
- ⁷D. Mendive-Tapia, M. Vacher, M. Bearpark, and M. A. Robb, *J. Chem. Phys.* **139**, 044110 (2013).
- ⁸Z. Li, O. Vendrell, and R. Santra, *Phys. Rev. Lett.* **115**, 143002 (2015).
- ⁹M. Vacher, L. Steinberg, A. J. Jenkins, M. J. Bearpark, and M. A. Robb, *Phys. Rev. A* **92**, 040502 (2015).
- ¹⁰V. Despre, A. Marciniak, V. Lorient, M. C. E. Galbraith, A. Rouze e, M. J. J. Vrakking, Lépine, F., and A. I. Kuleff, *J. Phys. Chem. Lett.* **6**, 426 (2015).
- ¹¹C. Arnold, O. Vendrell, and R. Santra, *Physical Review A* **95**, 033425 (2017).
- ¹²H. Wang, S. I. Bokarev, S. G. Aziz, and O. Kühn, *Phys. Rev. Lett.* **118**, 023001 (2017).
- ¹³H. Wang, S. I. Bokarev, S. G. Aziz, and O. Kühn, *Mol. Phys.* **115**, 1898 (2017).
- ¹⁴V. May and O. Kühn, *Charge and Energy Transfer Dynamics in Molecular Systems* (Wiley-VCH, Weinheim, 2011).
- ¹⁵J. C. Tremblay, S. Klinkusch, T. Klamroth, and P. Saalfrank, *J. Chem. Phys.* **134**, 044311 (2011).
- ¹⁶T. Kato, T. Oyamada, H. Kono, and S. Koseki, *Prog. Theor. Phys. Supplement* **196**, 16 (2012).
- ¹⁷W. Jin, F. Rupp, K. Chevalier, M. M. N. Wolf, M. C. Rojas, G. Lefkidis, H.-J. Krüger, R. Diller, and W. Hübner, *Phys. Rev. Lett.* **109**, 267209 (2012).
- ¹⁸P.-A. Malmqvist, A. Rendell, and B. O. Roos, *J. Phys. Chem.* **94**, 5477 (1990).
- ¹⁹B. A. Heß, C. M. Marian, U. Wahlgren, and O. Gropen, *Chem. Phys. Lett.* **251**, 365 (1996).
- ²⁰G. Hermann and J. C. Tremblay, *J. Phys. Chem. C* **119**, 25606 (2015).
- ²¹S. Mukamel, *Principles of Nonlinear Optical Spectroscopy* (Oxford Univ. Press, New York, 1999).
- ²²J. Stöhr, *NEXAFS Spectroscopy* (Springer-Verlag, Berlin, New York, 1992).
- ²³S. I. Bokarev, M. Dantz, E. Suljoti, O. Kühn, and E. F. Aziz, *Phys. Rev. Lett.* **111**, 083002 (2013).
- ²⁴K. Atak, S. I. Bokarev, M. Gotz, R. Golnak, K. M. Lange, N. Engel, M. Dantz, E. Suljoti, O. Kühn, and E. F. Aziz, *J. Phys. Chem. B* **117**, 12613 (2013).
- ²⁵R. Golnak, S. I. Bokarev, R. Seidel, J. Xiao, G. Grell, K. Atak, I. Unger, S. Thürmer, S. G. Aziz, O. Kühn, B. Winter, and E. F. Aziz, *Sci. Rep.* **6**, 24659 (2016).
- ²⁶M. Douglas and N. M. Kroll, *Ann. Phys.* **82**, 89 (1974), 02101.
- ²⁷F. Aquilante, J. Autschbach, R. K. Carlson, L. F. Chibotaru, M. G. Delcey, L. De Vico, I. F. Galván, N. Ferré, L. M. Frutos, L. Gagliardi, M. Garavelli, A. Giussani, C. E. Hoyer, G. Li Manni, H. Lischka, D. Ma, P. A. Malmqvist, T. Müller, A. Nenov, M. Olivucci, T. B. Pedersen, D. Peng, F. Plasser, B. Pritchard, M. Reiher, I. Rivalta, I. Schapiro, J. Segarra-Martí, M. Stenrup, D. G. Truhlar, L. Ungur, A. Valentini, S. Vancoillie, V. Veryazov, V. P. Vysotskiy, O. Weingart, F. Zapata, and R. Lindh, *J. Comput. Chem.* **37**, 506 (2016).
- ²⁸B. O. Roos, R. Lindh, P.-A. Malmqvist, V. Veryazov, and P.-O. Widmark, *J. Phys. Chem. A* **108**, 2851 (2004).
- ²⁹B. O. Roos, R. Lindh, P.-A. Malmqvist, V. Veryazov, and P.-O. Widmark, *J. Phys. Chem. A* **109**, 6575 (2005).
- ³⁰M. Ohno, *J. El. Spec. Rel. Phen.* **171**, 1 (2009).
- ³¹M. Vacher, M. J. Bearpark, M. A. Robb, and J. P. Malhado, *Phys. Rev. Lett.* **118**, 083001 (2017).
- ³²M. N. Piancastelli, G. Goldsztejn, T. Marchenko, R. Guillemin, R. K. Kushawaha, L. Journel, S. Carniato, J.-P. Rueff, D. Céolin, and M. Simon, *J. Phys. B* **47**, 124031 (2014).